Envelope-Detection-Based Accurate Small-Signal Modeling of Series Resonant Converters

Soumitro Vyapari, Viju Nair R, *Member, IEEE*, and Goutam Ghosh

***Abstract*—Resonant converters have many desirable characteristics, such as high efficiency, low component count, and low electromagnetic interference production. The resonance phenomenon that enables this also makes their design and control a challenging process. Attempts have been made to determine the small-signal control-to-output dynamics for resonant converters; however, they either involve complex mathematics or numerical solutions, which do not provide much insights and make it difficult to design controllers. This article uses fundamental harmonic approximation to model the different stages of a series resonant converter. Herein, the small-signal perturbations in control variable, i.e., switching frequency, result in perturbations in inductor current envelope that is analyzed in the Laplace domain. This current envelope is then used to analytically derive the control-to-output transfer function for the series resonant converter. The modeling process is verified and validated by comparing the analytical frequency response with that obtained from Simulink simulation and experimental results. For wide output voltage application designs, the system performance and stability vary with the changing operating point. An example demonstrating the utility of the developed model in analyzing such systems is also presented.**

***Index Terms*—Fundamental harmonic approximation, resonant converters, series resonant converter (SRC), small signal.**

I. Introduction

DC–DC converters find wide application in portable electronics [1], solid-state transformers (SSTs) [2], medium-voltage motor drives [3], electric vehicle battery charging systems [4], and telecommunication industry [5].

Most dc–dc converters can be categorized as either pulsewidth modulation (PWM) converters or resonant converters. Resonant converters have become a popular choice for many power electronics applications because they offer several advantages over traditional hard-switching PWM converters, such as zero-voltage-switching operation [6], low switching losses, high-frequency operation, reduced size of isolating transformers, and low electromagnetic interference production. Bidirectional resonant converters form an attractive topology for various smart grid applications such as vehicle-to-grid power flow [7].

Most applications require a regulated output voltage; hence, small-signal modeling of any converter becomes indispensable for controller design. The modeling and control of PWM converters have been widely studied in the literature. Techniques such as circuit averaging [8] and average switch model [9] have been developed for both the continuous and discontinuous modes of operation of PWM converters. Models for special control schemes, such as unified model [10] for current programmed control and describing function method [11] for V^2 control, have also been proposed in the literature. Hence, due to extensive research in this area, the design and control of PWM converters have become a simplified process. This, however, is not the case with resonant converters. Resonant converters have large sinusoidal variations in inductor currents and capacitor voltages, which is in contrast with PWM converters that have a dominant dc component in their state variables with a small ac ripple. Hence, it becomes difficult to use the inductor volt–second balance and capacitor charge balance for deriving the relevant transfer functions in resonant converters.

The series resonant converter (SRC) and the parallel resonant converter (PRC) are among the simplest resonant converter topologies, and several methods have been proposed in the literature to model them. The exact time-domain analysis of resonant converters has been presented in the literature [12]. The developed control-to-output and input-to-output transfer functions are shown to match closely with experimental results. However, the method requires a numerical solution and does not provide a simple approach for the controller design process. Sampled-data-based methods have also been proposed for the resonant converter [13], [14] and are able to predict the dynamics; however, it is difficult to get physical insights in the behavior of SRC from sampled-data methods. Extended describing functions (EDFs) are also used to model resonant converters [15] and are among the most successful and insightful methods available. In this method, the nonlinear terms appearing in the state-space representation are approximated with their fundamental component to arrive at a linear model. The model leads to a fifth-order equivalent circuit for the SRC that can be used to simulate the Bode plot of required transfer functions. However, the method involves fair amount of mathematics to arrive at the solution. Also, it is difficult to gain insight into how the circuit parameters affect the dynamic response by directly examining the equivalent circuit. This is partly due

Manuscript received 4 October 2022; revised 4 January 2023 and 3 March 2023; accepted 10 April 2023. Date of publication 20 April 2023; date of current version 19 May 2023. This work was supported in part by the Science and Engineering Research Board, New Delhi, India, under Grant CRG/2022/006124 and in part by the Indian Institute of Technology Tirupati, India. Recommended for publication by Associate Editor J. Lam. *(Corresponding author: Viju Nair R.)*

Soumitro Vyapari was with the Department of Electrical Engineering, Indian Institute of Technology Tirupati, Tirupati 517619, India. He is now with Texas Instruments, Bengaluru 560093, India (e-mail: ee18b032@iittp.ac.in).

Viju Nair R and Goutam Ghosh are with the Department of Electrical Engineering, Indian Institute of Technology Tirupati, Tirupati 517619, India (e-mail: vnr@iittp.ac.in; ee20s502@iittp.ac.in).

Color versions of one or more figures in this article are available at https://doi.org/10.1109/TPEL.2023.3268635.

Digital Object Identifier 10.1109/TPEL.2023.3268635

to the fifth order of the circuit and partly due to encoding of circuit parameters into coefficients of controlled voltage and current sources. Attempts have been made to simplify the solution by representing the resonant capacitor as an equivalent inductor with respect to modulating frequency [16]. However, it is still based on the equivalent circuit model of the EDF developed in [15] and requires a thorough understanding of the complex mathematics involved. An analytical closed-form sampled-data-based model of the SRC has also been presented in [17]. The nonlinear state-space representation of SRC for different switch configurations is combined to form a discrete model, which is then perturbed to obtain the small-signal model. However, only the input-to-output transfer function is derived in the z-domain having complicated functions as its coefficients. Recently, a general multifrequency small-signal model of resonant converters has been proposed [18]. The model derives gains between important quantities, such as input frequency, inverter voltage, and rectifier current. The gains are then combined in a block diagram, and Mason's gain formula is used to derive the required transfer functions. The model is able to accurately predict the small-signal dynamics for a variety of converter topologies; however, it requires the derivation of several gains, and significant simplification is required to arrive at a form that can be easily interpreted for controller design.

One method to perform system identification is subjecting the system input to sinusoidal perturbations of angular frequency w_p and observing the system output response. For a linear-time-invariant system, the output also varies with the same frequency w_p but with a different amplitude and phase, which can be captured using the system transfer function. For the SRC, if the small-signal relation between the system input, i.e., switching frequency, and the system output, i.e., output voltage, is assumed to be linear, then the same method can be applied to determine the small-signal control-to-output transfer function for the SRC. In this article, the above approach has been followed. First, the switching frequency is perturbed about its quiescent value, which results in perturbations in the inductor current and the capacitor voltage. Those resulting perturbations are analytically calculated to obtain the relevant small-signal transfer functions. The main contributions of this article are as follows.

1) The proposed method bypasses the fifth-order equivalent circuit generation and simplification process required by the EDF and directly models the system in the Laplace domain using the approximation that the frequencies of interest in the transfer function are much smaller than the switching frequency to arrive at a simplified third-order transfer function. Thus, this method significantly reduces the mathematical complexity found in the EDF, while still providing insights into the converter dynamics.
2) The proposed method is applicable to other frequency-modulated (FM) converters, such as PRC, *LLC*, etc. Thus, although the EDF can be used for accurate modeling of resonant converters, the proposed method can provide benefits in terms of mathematical effort required to arrive at the model and the insights gained from the simple transfer function for controller design of various other topologies.

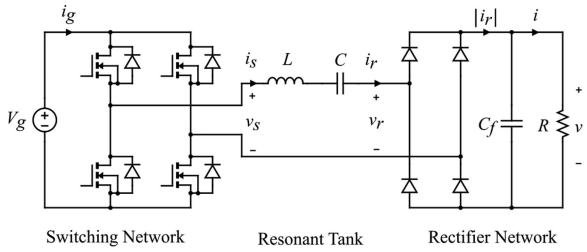

Fig. 1. Schematic of the SRC.

3) The model is able to capture the beat frequency dynamics. The origin and location of beat frequency have been explained both at an intuitive level and also analytically from the resulting transfer function.
4) The developed model is analyzed to observe the dynamic performance and stability over large operating range, demonstrating its easiness and utility for wide output voltage application designs.

The rest of this article is organized as follows. Section II describes the small-signal modeling of various stages of SRC. Section III presents the derivation of small-signal control-to-output transfer function of SRC. Section IV includes simulation and experimental results, which validate the modeling process. Section V presents the performance analysis of SRC with the derived model. Finally, Section VI concludes this article. The derivation of input-to-output transfer function and input and output impedances have been presented in the Appendixes for reference.

II. Small-Signal Modeling of the SRC

As shown in Fig. 1, the SRC can be qualitatively divided into three stages [19]. The first stage consists of the dc input source V_g and the switching network that outputs a square wave of amplitude V_g. The output current and voltage of the switching network are represented as $i_s(t)$ and $v_s(t)$, respectively. The second stage consists of the resonant tank circuit formed by L and C in series. The third stage consists of the rectifier network and load impedance. The input current and voltage of the rectifier network are represented as $i_r(t)$ and $v_r(t)$, respectively. For the SRC, both $i_s(t)$ and $i_r(t)$ represent the same quantity, i.e., inductor current. Each of the stages is modeled separately with emphasis on small-signal dynamics. This allows for reuse of the switching network or rectifier stage model for other resonant converter topologies since these stages usually remain common.

A. Switching Network

The square wave voltage source can be replaced with its fundamental harmonic. This is motivated by the fact that if the frequency of switching network f_s is close to the resonant frequency of LC tank circuit, then the tank circuit will respond strongly to the fundamental harmonic only while attenuating all higher order harmonics present in input square wave. The square wave with an angular frequency Ω_s and amplitude V_g

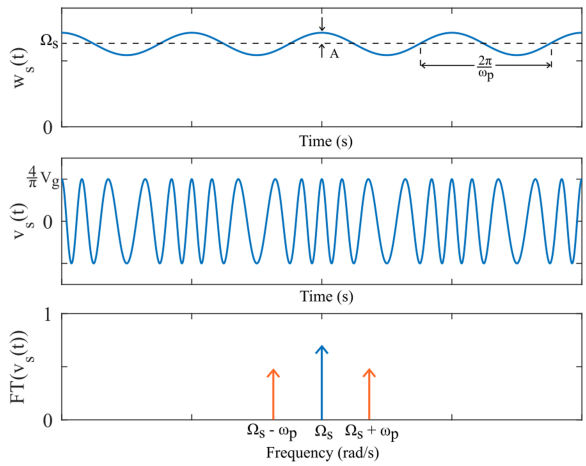

Fig. 2. Top: Instantaneous angular frequency. Middle: FM voltage source. Bottom: Fourier transform of $v_s(t)$ valid only for $\frac{A}{w_p} << 2\pi$.

can be represented using Fourier series as follows:

$$v_s(t) = \frac{4V_g}{\pi} \sum_{n=1,3,5,\ldots} \frac{1}{n} \cos(n\Omega_s t). \tag{1}$$

Hence, using fundamental harmonic approximation, the switching network can be modeled as a sinusoidal voltage source of frequency f_s and amplitude $\frac{4V_g}{\pi}$.

To study the effect of control input, i.e., instantaneous switching frequency, a perturbation in switching frequency can be provided, and the resulting switching network output $v_s(t)$ can be modeled by a suitable controlled voltage source. The same has been done below by describing the switching frequency variation as an equivalent phase variation. If the phase of the cosine $v_s(t) = \frac{4V_g}{\pi} \cos(\Omega_s t)$ is perturbed with some control signal $\theta(t) = \int_0^t m(t)\, dt$, then the switching network appears as an FM voltage source $v_s(t)$ [20]

$$v_s(t) = \frac{4V_g}{\pi} \cos(\Omega_s t + \theta(t)). \tag{2}$$

The instantaneous angular frequency of this FM voltage source is given by

$$w_s(t) = \frac{d}{dt}(\Omega_s t + \theta(t)) \tag{3}$$

$$w_s(t) = \Omega_s + \frac{d\theta(t)}{dt} = \Omega_s + m(t). \tag{4}$$

For a sinusoidal perturbation $m(t) = A\cos(w_p t)$, the instantaneous angular frequency is given by $w_s(t) = \Omega_s + A\cos(w_p t)$. Here, A is the absolute frequency variation about the quiescent angular frequency Ω_s and w_p is the rate of variation of the instantaneous angular frequency. Such an FM voltage source output waveform is presented in Fig. 2.

The voltage source $v_s(t)$ described in (2) is difficult to analyze with linear theory. To make the analysis tractable, small-signal approximation for the perturbations is assumed. If $\theta(t) << 2\pi$ or $\int_0^t m(t)\, dt << 2\pi$, then

$$v_s(t) = \frac{4V_g}{\pi}(\cos(\Omega_s t)\cos(\theta(t)) - \sin(\Omega_s t)\sin(\theta(t))) \tag{5}$$

$$v_s(t) = \frac{4V_g}{\pi}(\cos(\Omega_s t) - \theta(t)\sin(\Omega_s t)). \tag{6}$$

Now, if $m(t)$ is replaced with a specific sinusoidal perturbation as before and θ is substituted in terms of $m(t)$, then

$$v_s(t) = \frac{4V_g}{\pi}(\cos(\Omega_s t) - \frac{A}{w_p}\sin(w_p t)\sin(\Omega_s t)) \tag{7}$$

$$v_s(t) = \frac{4V_g}{\pi}(\cos(\Omega_s t) - \frac{A}{2w_p}\cos((\Omega_s - w_p)t) + \frac{A}{2w_p}\cos((\Omega_s + w_p)t)). \tag{8}$$

As can be observed from (8), the FM voltage source can be equivalently split into three voltage sources, each with a different frequency. If this source is applied to a passive RLC network, the current and voltage waveforms can be expected to be having the three frequencies. This key observation allows for a solution to be assumed for the differential equations of the SRC, as shown in the next sections. The particular frequencies $(\Omega_s - w_p)$ and $(\Omega_s + w_p)$ lead to the interesting phenomenon of beat dynamics observed in resonant converters [21]. If the FM voltage source is applied to a passive circuit formed by series L, C, and R, the circuit responds strongly whenever $\Omega_s - \omega_p = \Omega_0$ or $\Omega_s + w_p = \Omega_0$, where Ω_0 is the angular resonant frequency. This happens because at that w_p, one of the driving sources starts driving the LC tank at its resonant frequency. Thus, the small-signal control-to-output transfer function for series L–C–R will have a peak at $w_p = |\Omega_s - \Omega_0|$. Note that, here, the output is assumed to be across the resistor R. In the case of SRC, as will be shown, the rectifier network cannot be represented as a simple resistor; however, the LC tank still responds strongly whenever excited with a perturbation $m(t) = A\cos(w_p t)$, where $w_p = |\Omega_s - \Omega_0|$. This frequency is known as the beat frequency.

B. Tank Network and Equivalent Circuit

The tank circuit consists of the resonant inductor in series with the resonant capacitor. Since both are linear circuit elements, they appear as it is for both large- and small-signal dynamics.

C. Rectifier Input

If the SRC is operated at a quiescent frequency Ω_s, the rectifier network and load stage can be represented with an equivalent resistance $R_{\text{eq}} = \frac{8}{\pi^2}R$, as shown in [1]. It, however, cannot be used for the dynamic model, because it neglects the interaction between the filter capacitor C_f and the tank network. This can be better observed from the simulation results presented in Fig. 3. Herein, the control input, i.e., switching frequency, is perturbed by a sinusoidal variation about its quiescent value Ω_s. This results in sinusoidal perturbations in inductor current envelope, as shown in Fig. 3(b). These perturbations are present in the rectified current as well, which flows through the parallel combination of R and C_f and results in output voltage perturbations, as shown in Fig. 3(c). These output voltage perturbations, which may not be in phase with current envelope perturbations, are reflected back on the input side of the rectifier in the form of rectifier voltage perturbations, as shown in Fig. 3(d). Thus, although

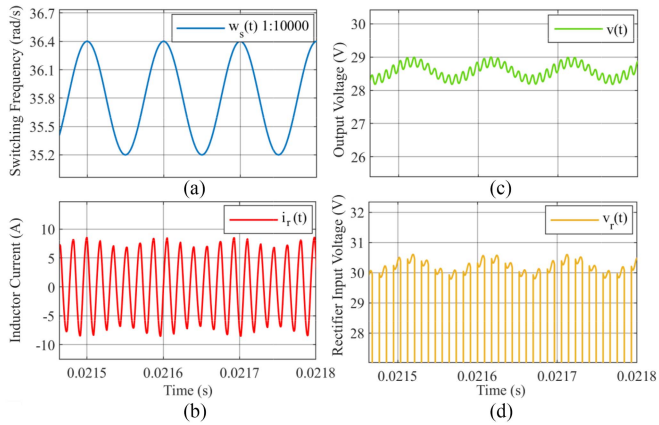

Fig. 3. (a) Instantaneous angular switching frequency. (b) Inductor current. (c) Output voltage. (d) Rectifier input voltage.

$i_r(t)$ and $v_r(t)$ are in phase, the sinusoidal perturbations in their envelopes may not be in phase, and hence, the rectifier cannot be replaced with an equivalent resistance in the small-signal model. This out-of-phase characteristics between the current and voltage perturbations is precisely due to the interaction between the tank current and the filter capacitor C_f.

The previous paragraph suggests that an explicit representation of the rectifier input voltage may result in a more accurate model than the equivalent resistance model. The rectifier voltage $v_r(t)$ can be represented as follows:

$$v_r(t) = v(t)\text{sign}(i_r(t)) \tag{9}$$

where $v(t)$ is the output voltage and $i_r(t)$ is the inductor current. The rectifier input voltage is the same as the output voltage, except for the sign that is the same as that of inductor current. Furthermore, the inductor current can be approximated by a general sinusoid $i_r(t) = I_c(t)\cos(\Omega_s t) + I_s(t)\sin(\Omega_s t)$ with time-varying amplitude representing the small-signal variations. The rectifier input voltage can be approximated as

$$v_r(t) = \frac{4}{\pi}v(t)\frac{I_c(t)\cos(\Omega_s t) + I_s(t)\sin(\Omega_s t)}{\sqrt{I_c(t)^2 + I_s(t)^2}}. \tag{10}$$

The term $\frac{4}{\pi}$ in (10) signifies that the square wave $v_r(t)$ is approximated by its fundamental. Since each of the terms $v(t), I_c(t)$, and $I_s(t)$ is made up of dc and small-signal values, i.e., $v(t) = v_{\text{dc}} + v_{\text{ss}}(t)$, $I_c(t) = I_{c\_\text{dc}} + I_{c\_\text{ss}}(t)$ and $I_s(t) = I_{s\_\text{dc}} + I_{s\_\text{ss}}(t)$, the $\cos(\Omega_s t)$ coefficient becomes

$$\begin{aligned}\frac{I_c(t)}{\sqrt{I_c(t)^2 + I_s(t)^2}} &= \frac{I_{c\_\text{dc}} + I_{c\_\text{ss}}}{\sqrt{(I_{c\_\text{dc}} + I_{c\_\text{ss}})^2 + (I_{s\_\text{dc}} + I_{s\_\text{ss}})^2}} \\ &= \frac{I_{c\_\text{dc}} + I_{c\_\text{ss}}}{\sqrt{I_{c\_\text{dc}}^2 + I_{s\_\text{dc}}^2}\sqrt{1 + \frac{2(I_{c\_\text{dc}}I_{c\_\text{ss}} + I_{s\_\text{dc}}I_{s\_\text{ss}})}{I_{c\_\text{dc}}^2 + I_{s\_\text{dc}}^2}}}\end{aligned} \tag{11}$$

where the denominator has been first expanded, higher order terms neglected, and $\sqrt{I_{c\_\text{dc}}^2 + I_{s\_\text{dc}}^2}$ taken common. Equation (11) can be further simplified by using the approximation $\frac{1}{\sqrt{1+x}} \approx 1 - \frac{x}{2}$ for $x << 1$ to give

$$\begin{aligned}&\frac{I_{c\_\text{dc}} + I_{c\_\text{ss}}}{\sqrt{I_{c\_\text{dc}}^2 + I_{s\_\text{dc}}^2}}\left(1 - \frac{I_{c\_\text{dc}}I_{c\_\text{ss}} + I_{s\_\text{dc}}I_{s\_\text{ss}}}{I_{c\_\text{dc}}^2 + I_{s\_\text{dc}}^2}\right) \\ &= \frac{I_{c\_\text{dc}} + I_{c\_\text{ss}} - \alpha^2 I_{c\_\text{ss}} - \alpha\beta I_{s\_\text{ss}}}{\sqrt{I_{c\_\text{dc}}^2 + I_{s\_\text{dc}}^2}}\end{aligned} \tag{12}$$

where $\alpha = \frac{I_{c\_\text{dc}}}{\sqrt{I_{c\_\text{dc}}^2 + I_{s\_\text{dc}}^2}}$ and $\beta = \frac{I_{s\_\text{dc}}}{\sqrt{I_{c\_\text{dc}}^2 + I_{s\_\text{dc}}^2}}$.

Similar simplification can be performed for the $\sin(\Omega_s t)$ coefficient as well. Hence, (10) can be perturbed as

$$\begin{aligned}v_r(t) = &\\ &\frac{4}{\pi}(v_{\text{dc}} + v_{\text{ss}})\frac{(I_{c\_\text{dc}} + I_{c\_\text{ss}} - \alpha^2 I_{c\_\text{ss}} - \alpha\beta I_{s\_\text{ss}})}{\sqrt{I_{c\_\text{dc}}^2 + I_{s\_\text{dc}}^2}}\cos(\Omega_s t) \\ &+ \frac{4}{\pi}(v_{\text{dc}} + v_{\text{ss}})\frac{(I_{s\_\text{dc}} + I_{s\_\text{ss}} - \beta^2 I_{s\_\text{ss}} - \alpha\beta I_{c\_\text{ss}})}{\sqrt{I_{c\_\text{dc}}^2 + I_{s\_\text{dc}}^2}}\sin(\Omega_s t).\end{aligned} \tag{13}$$

The following results from the steady-state solution of SRC can be used [1] for the simplification of (13). The dc value of output load current $i(t)$ is equal to the dc value of rectified current $|i_r(t)|$; this is because the filter capacitor C_f acts as open for dc. The dc value of rectified current can be found as follows. First, the perturbations in switching frequency are turned OFF; this causes the small-signal perturbations in current envelope, i.e., $I_{c\_\text{ss}}(t)$ and $I_{s\_\text{ss}}(t)$, to become zero. Now, $|i_r(t)|$ reduces to $|I_{c\_\text{dc}}\cos(\Omega_s t) + I_{s\_\text{dc}}\sin(\Omega_s t)|$, which has a dc value of $\frac{2}{\pi}\sqrt{I_{c\_\text{dc}}^2 + I_{s\_\text{dc}}^2}$, as can be found by averaging $|i_r(t)|$ over one switching cycle

$$i(t) = i_{\text{dc}} + i_{\text{ss}}(t) \tag{14}$$

$$i_{\text{dc}} = \frac{2}{\pi}\sqrt{I_{c\_\text{dc}}^2 + I_{s\_\text{dc}}^2}. \tag{15}$$

Also, the dc load current is related to the dc load voltage by R

$$\frac{v_{\text{dc}}}{i_{\text{dc}}} = R. \tag{16}$$

Using (15), (16), and $R_{\text{eq}} = \frac{8}{\pi^2}R$, we obtain

$$\frac{4}{\pi}\frac{v_{\text{dc}}}{\sqrt{I_{c\_\text{dc}}^2 + I_{s\_\text{dc}}^2}} = R_{\text{eq}}. \tag{17}$$

Now, $v_r(t)$ in (13) can be linearized in terms of small-signal perturbations by neglecting higher order terms and using (17) and $\alpha^2 + \beta^2 = 1$ to simplify the results as

$$\begin{aligned}v_r(t) = &\left(R_{\text{eq}}I_{c\_\text{dc}} + \frac{4}{\pi}\alpha v_{\text{ss}} - \alpha\beta R_{\text{eq}}I_{s\_\text{ss}}\right. \\ &\left. + \beta^2 R_{\text{eq}}I_{c\_\text{ss}}\right)\cos(\Omega_s t) + \left(R_{\text{eq}}I_{s\_\text{dc}} + \frac{4}{\pi}\beta v_{\text{ss}}\right. \\ &\left. + \alpha^2 R_{\text{eq}}I_{s\_\text{ss}} - \alpha\beta R_{\text{eq}}I_{c\_\text{ss}}\right)\sin(\Omega_s t).\end{aligned} \tag{18}$$

D. Rectifier Output

The output of rectifier can be modeled by observing that the rectifier rectifies the inductor current $i_r(t)$. This rectified current $|i_r(t)|$ also has the same envelope perturbations as that of $i_r(t)$. The second harmonic component of $|i_r(t)|$ at the angular frequency of $2\Omega_s$ can be neglected since it flows mainly through the filter capacitor C_f that is designed to produce low output voltage ripple at $2\Omega_s$ frequency. Hence, only the dc and small-signal components of $|i_r(t)|$ are left, which flow through the parallel combination of C_f and R producing the output voltage $v(t)$. Using the circuit of SRC in Fig. 1, we have

$$C_f\frac{dv(t)}{dt}+\frac{v(t)}{R}=|i_r(t)| \tag{19}$$

$$|i_r(t)|=|I_c(t)\cos(\Omega_s t)+I_s(t)\sin(\Omega_s t)|\approx\frac{2}{\pi}\sqrt{I_c(t)^2+I_s(t)^2} \tag{20}$$

where $|i_r(t)|$ is first represented with its Fourier series and truncated to its dc component for analytical tractability. Note that, here, the small-signal perturbations in $I_c(t)$ and $I_s(t)$ are assumed to be slow compared to switching frequency Ω_s and, hence, appear as dc while averaging $|i_r(t)|$ over one switching period

$$C_f\frac{dv(t)}{dt}+\frac{v(t)}{R}=\frac{2}{\pi}(\alpha I_{c\_ss}(t)+\beta I_{s\_ss}(t)+\sqrt{I_{c\_dc}^2+I_{s\_dc}^2}) \tag{21}$$

which has been simplified assuming $I_{c\_ss}(t)<<I_{c\_dc}$ and $I_{s\_ss}(t)<<I_{s\_dc}$ and using the identity $\sqrt{1+x}\approx 1+\frac{x}{2}$ for $x\approx 0$. Using (21), the output voltage in the Laplace domain can be found as

$$v(s)=\frac{2}{\pi}\frac{R}{(1+RC_f s)}\left(\alpha I_{c\_ss}(s)+\beta I_{s\_ss}(s)+\frac{\sqrt{I_{c\_dc}^2+I_{s\_dc}^2}}{s}\right). \tag{22}$$

The dc value of $v(t)$ can be found in the following manner. First, the perturbations in switching frequency are turned OFF. This causes the small-signal perturbations in current envelope, i.e., $I_{c\_ss}(t)$ and $I_{s\_ss}(t)$, to go to zero in (22). Now, the dc value of $v(t)$ can be found to be $v_{dc}=\frac{2}{\pi}R\sqrt{I_{c\_dc}^2+I_{s\_dc}^2}$ by applying the final value theorem, while $v_{ss}(s)$ is given as

$$v_{ss}(s)=\frac{2}{\pi}\frac{R}{(1+RC_f s)}(\alpha I_{c\_ss}(s)+\beta I_{s\_ss}(s)). \tag{23}$$

III. Proposed Small-Signal Transfer Functions of SRC

In this section, the small-signal control-to-output transfer function of SRC is developed by substituting the previously developed network models into the differential equations of SRC.

A. Large-Signal State Equations

From the circuit of SRC in Fig. 1, we have

$$v_s(t)=L\frac{di_r(t)}{dt}+\frac{1}{C}\int_0^t i_r(t)\,dt+v_r(t) \tag{24}$$

$$\frac{dv_s(t)}{dt}=L\frac{d^2i_r(t)}{dt^2}+\frac{i_r(t)}{C}+\frac{dv_r(t)}{dt}. \tag{25}$$

Substituting $v_s(t)$ from (6), and $i_r(t)=(I_{c\_dc}+I_{c\_ss})\cos(\Omega_s t)+(I_{s\_dc}+I_{s\_ss})\sin(\Omega_s t)$ and $v_r(t)$ from (18) into (25), and performing harmonic balance by separating the sine $(\sin(\Omega_s t))$ and cosine $(\cos(\Omega_s t))$ components, for dc terms, we have

$$0=-LI_{c\_dc}\Omega_s^2+\frac{I_{c\_dc}}{C}+\Omega_s R_{eq}I_{s\_dc} \tag{26}$$

$$-\frac{4}{\pi}V_g\Omega_s=-LI_{s\_dc}\Omega_s^2+\frac{I_{s\_dc}}{C}-\Omega_s R_{eq}I_{c\_dc} \tag{27}$$

and for small-signal terms, we have

$$\begin{aligned}-\frac{4}{\pi}V_g\Omega_s\int_0^t m(t)\,dt=&-L\Omega_s^2I_{c\_ss}(t)+L\frac{d^2I_{c\_ss}(t)}{dt^2}\\&+2L\Omega_s\frac{dI_{s\_ss}(t)}{dt}+\frac{I_{c\_ss}(t)}{C}\\&+\left(\frac{4}{\pi}\alpha\frac{dv_{ss}}{dt}+\beta^2R_{eq}\frac{dI_{c\_ss}}{dt}-\alpha\beta R_{eq}\frac{dI_{s\_ss}}{dt}\right)\\&+\Omega_s\left(\frac{4}{\pi}\beta v_{ss}+\alpha^2R_{eq}I_{s\_ss}-\alpha\beta R_{eq}I_{c\_ss}\right)\end{aligned} \tag{28}$$

$$\begin{aligned}-\frac{4}{\pi}V_g m(t)=&-L\Omega_s^2I_{s\_ss}(t)+L\frac{d^2I_{s\_ss}(t)}{dt^2}\\&-2L\Omega_s\frac{dI_{c\_ss}(t)}{dt}+\frac{I_{s\_ss}(t)}{C}\\&+\left(\frac{4}{\pi}\beta\frac{dv_{ss}}{dt}+\alpha^2R_{eq}\frac{dI_{s\_ss}}{dt}-\alpha\beta R_{eq}\frac{dI_{c\_ss}}{dt}\right)\\&-\Omega_s\left(\frac{4}{\pi}\alpha v_{ss}+\beta^2R_{eq}I_{c\_ss}-\alpha\beta R_{eq}I_{s\_ss}\right).\end{aligned} \tag{29}$$

Equations (26) and (27) can be solved to calculate the dc quantities as

$$I_{c\_dc}=\frac{4}{\pi}V_g\frac{R_{eq}}{X_{eq}^2+R_{eq}^2} \tag{30}$$

$$I_{s\_dc}=\frac{4}{\pi}V_g\frac{X_{eq}}{X_{eq}^2+R_{eq}^2} \tag{31}$$

where $R_{eq}=\frac{8}{\pi^2}R$ and $X_{eq}=(L\Omega_s-\frac{1}{C\Omega_s})$.

Equations (28) and (29) are ordinary differential equations (ODEs) and can be solved in the Laplace domain. Converting both equations to the Laplace domain and grouping $I_{c\_ss(s)}$ and $I_{s\_ss}(s)$ terms together gives

$$\begin{aligned}-\frac{4}{\pi}V_g\Omega_s\frac{m(s)}{s}=&\left(-L\Omega_s^2+Ls^2+\frac{1}{C}+R_{eq}(\beta^2s-\alpha\beta\Omega_s)\right.\\&\left.+\frac{R_{eq}}{RC_fs+1}\left(\alpha^2s+\alpha\beta\Omega_s\right)\right)I_{c\_ss}(s)+\left(2L\Omega_s s\right.\\&\left.+R_{eq}(\alpha^2\Omega_s-\alpha\beta s)+\frac{R_{eq}}{RC_fs+1}\left(\alpha\beta s+\beta^2\Omega_s\right)\right)I_{s\_ss}(s)\end{aligned} \tag{32}$$

$$-\frac{4}{\pi}V_g m(s) = -\Bigg(2L\Omega_s s + \frac{R_{\text{eq}}}{RC_f s+1}(\alpha^2\Omega_s - \alpha\beta s) + R_{\text{eq}}\left(\beta^2\Omega_s + \alpha\beta s\right)\Bigg)I_{c\_\text{ss}}(s) + \Bigg(-L\Omega_s^2 + Ls^2 + \frac{1}{C} + R_{\text{eq}}(\alpha^2 s + \alpha\beta\Omega_s) + \frac{R_{\text{eq}}}{RC_f s+1}\left(\beta^2 s - \alpha\beta\Omega_s\right)\Bigg)I_{s\_\text{ss}}(s) \tag{33}$$

where v_{ss} has been substituted in terms of I_{c_ss} and I_{s_ss} using (23). To make the analysis more tractable, (32) and (33) have been divided by Ω_s, and the approximation $\frac{s}{\Omega_s} \approx 0$ (i.e., perturbation frequency is much smaller than switching frequency) is used to reduce the equations to

$$-\frac{4}{\pi}V_g\frac{m(s)}{s} = \Bigg(-L\Omega_s + \frac{1}{C\Omega_s} - \alpha\beta R_{\text{eq}} + \alpha\beta\frac{R_{\text{eq}}}{RC_f s+1}\Bigg)I_{c\_\text{ss}}(s) + \Bigg(2Ls + \beta^2\frac{R_{\text{eq}}}{RC_f s+1} + \alpha^2 R_{\text{eq}}\Bigg)I_{s\_\text{ss}}(s) \tag{34}$$

$$-\frac{4}{\pi}\frac{V_g}{\Omega_s}m(s) = -\left(2Ls + \alpha^2\frac{R_{\text{eq}}}{RC_f s+1} + \beta^2 R_{\text{eq}}\right)I_{c\_\text{ss}}(s) + \left(-L\Omega_s + \frac{1}{C\Omega_s} + \alpha\beta R_{\text{eq}} - \alpha\beta\frac{R_{\text{eq}}}{RC_f s+1}\right)I_{s\_\text{ss}}(s). \tag{35}$$

The rationale behind assuming $\frac{s}{\Omega_s} \approx 0$ comes from the fact that most controller designs require an accurate control-to-output transfer function from dc to beat frequency. Since the beat frequency is usually a fraction of switching frequency, the approximation $\frac{s}{\Omega_s} << 1$ holds well till beat frequency. Now, once (32) and (33) are divided by Ω_s, the terms are grouped such that there are two similar order terms in each group, but one scaled by the factor $\frac{s}{\Omega_s}$. This allows neglecting the scaled term in comparison to the other.

Equations (34) and (35) can be solved to derive the perturbations in current envelopes I_{c_ss} and I_{s_ss} as

$$I_{c\_\text{ss}}(s) = \frac{4}{\pi}V_g\frac{\left(X_{\text{eq}} - \alpha\beta R_{\text{eq}} + \alpha\beta\frac{R_{\text{eq}}}{RC_f s+1}\right)}{\text{den}_1}m(s) \tag{36}$$

$$I_{s\_\text{ss}}(s) = -\frac{4}{\pi}V_g\frac{\left((L+\frac{1}{C\Omega_s^2})s + \beta^2 R_{\text{eq}} + \alpha^2\frac{R_{\text{eq}}}{RC_f s+1}\right)}{\text{den}_1}m(s) \tag{37}$$

where

$$\text{den}_1 = s\left(4L^2s^2 + 2R_{\text{eq}}Ls + X_{\text{eq}}^2 + \frac{R_{\text{eq}}}{RC_f s+1}(2Ls+R_{\text{eq}})\right) \tag{38}$$

and R_{eq} and X_{eq} are same as before.

If the instantaneous amplitude/envelope of $i_r(t)$ is represented by $I_e(t) = \sqrt{I_c(t)^2 + I_s(t)^2}$, then small-signal variation in envelope of $i_r(t)$, i.e., $\alpha I_{c\_\text{ss}}(t) + \beta I_{s\_\text{ss}}(t)$, due to the perturbation of angular switching frequency can be found as

$$\alpha I_{c\_\text{ss}}(s) + \beta I_{s\_\text{ss}}(s) = -\frac{4}{\pi}V_g\beta\frac{(L+\frac{1}{C\Omega_s^2})s}{\text{den}_1}m(s). \tag{39}$$

The small-signal transfer function from $m(s)$ to $v(s)$ can be derived by substituting (39) into (23) as

$$\frac{v_{\text{ss}}(s)}{m(s)} = \frac{K}{\text{den}_2} \tag{40}$$

where $K = -\frac{V_g}{\Omega_s}\frac{R_{\text{eq}}}{\sqrt{X_{\text{eq}}^2+R_{\text{eq}}^2}}X_{\text{eq}}(L\Omega_s + \frac{1}{C\Omega_s})$ and

$$\text{den}_2 = (4L^2s^2 + 2R_{\text{eq}}Ls + X_{\text{eq}}^2)(1+RC_f s) + R_{\text{eq}}(2Ls+R_{\text{eq}}). \tag{41}$$

Equation (40) presents the reduced-order small-signal control-to-output transfer function of SRC. The derivations of small-signal input-to-output transfer function, input impedance, and output impedance have been presented in the Appendixes. All the derived transfer functions have been presented in Table I for ease of reference.

The beat frequency can be approximately located from the resulting transfer function in (40). If the beat frequency $w_{\text{beat}} >> \frac{1}{RC_f}$, then the term $(1+RC_f s)$ can be taken common in the denominator and the term $\frac{2R_{\text{eq}}Ls}{(1+RC_f s)}$ can be neglected in comparison to $2R_{\text{eq}}Ls$ around the beat frequency; similarly, $\frac{R_{\text{eq}}^2}{(1+RC_f s)}$ can be neglected in comparison to X_{eq}^2 since R_{eq}^2 and X_{eq}^2 of similar order for switching frequencies not very close to the resonant frequency. The transfer function around the beat frequency can then be written as

$$\frac{v_{\text{ss}}(s)}{m(s)} = \frac{K}{(1+RC_f s)(4L^2s^2 + 2R_{\text{eq}}Ls + X_{\text{eq}}^2)}. \tag{42}$$

From the above equation, the beat frequency can be noted as natural frequency of complex conjugate poles, i.e., $w_{\text{beat}} = \sqrt{\frac{X_{\text{eq}}^2}{4L^2}} = |\frac{X_{\text{eq}}}{2L}| = \frac{1}{2}|\Omega_s - \frac{1}{LC\Omega_s}| = \frac{|\Omega_s^2-\Omega_0^2|}{2\Omega_s} = \frac{\Omega_s+\Omega_0}{2\Omega_s}|\Omega_s - \Omega_0|$. If Ω_s and Ω_0 are not very different, then the beat frequency is given approximately by $w_{\text{beat}} = |\Omega_s - \Omega_0|$. Similarly, for the quality factor Q, it can be noted that

TABLE I
SMALL-SIGNAL TRANSFER FUNCTIONS OF THE SRC

$\frac{v_{ss}(s)}{m(s)} = \frac{K}{(4L^2s^2+2R_{eq}Ls+X_{eq}^2)(1+RC_f s)+R_{eq}(2Ls+R_{eq})}$ $K = -\frac{V_g}{\Omega_s}\frac{R_{eq}}{\sqrt{X_{eq}^2+R_{eq}^2}}X_{eq}\left(L\Omega_s + \frac{1}{C\Omega_s}\right)$
$\frac{v_{ss}(s)}{V_{g\_ss}(s)} = \frac{K_1(X_{eq}^2+R_{eq}^2+2LR_{eq}s)}{(4L^2s^2+2R_{eq}Ls+X_{eq}^2)(1+RC_f s)+R_{eq}(2Ls+R_{eq})}$ $K_1 = \frac{R_{eq}}{\sqrt{R_{eq}^2+X_{eq}^2}}$
$Z_{\text{in}}(s) = \frac{\pi^2}{8}\frac{(4L^2s^2+2R_{eq}Ls+X_{eq}^2)(1+RC_f s)+R_{eq}(2Ls+R_{eq})}{2Ls(RC_f s+1)+\alpha^2 R_{eq}RC_f s+R_{eq}^2}$
$Z_{\text{out}}(s) = \frac{R(4L^2s^2+2R_{eq}Ls+X_{eq}^2)}{(4L^2s^2+2R_{eq}Ls+X_{eq}^2)(1+RC_f s)+R_{eq}(2Ls+R_{eq})}$

TABLE II
SIMULATION PARAMETERS OF THE SRC

Parameter	Value
Input Nominal Voltage	400 V
Resonant Frequency	50.2 kHz
Resonant Inductor (L)	197 μH
Resonant Capacitor (C)	51 nF
Load Resistor (R)	15.5 Ω
Filter Capacitor (C_f)	32 μF

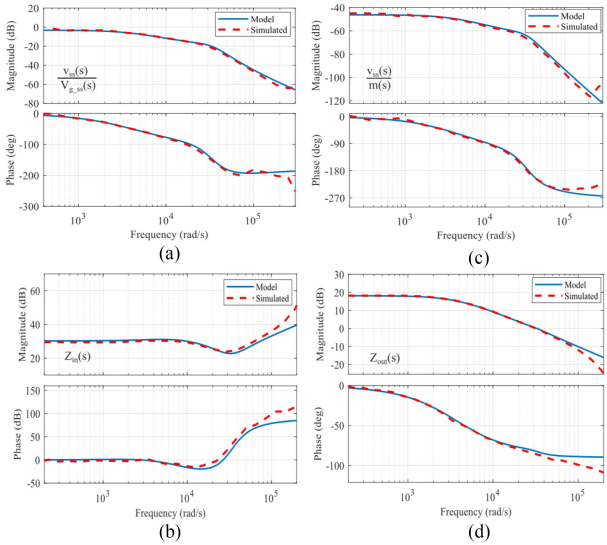

Fig. 4. Comparison of analytical model with simulated data for $f_s = 0.9f_o$. (a) Input to output transfer function. (b) Z_{in}. (c) Control to output transfer function. (d) Z_{out}.

$\frac{1}{Qw_{\text{beat}}} = \frac{2L}{Q|X_{\text{eq}}|} = \frac{2R_{\text{eq}}L}{X_{\text{eq}}^2}$, which gives $Q = \frac{|X_{\text{eq}}|}{R_{\text{eq}}} = \frac{|L\Omega_s - \frac{1}{C\Omega_s}|}{R_{\text{eq}}}$ after rearranging.

IV. SIMULATION AND EXPERIMENTAL RESULTS

The MATLAB Simulink tool was used to derive the Bode plot for the control-to-output transfer function, input-to-output transfer function, and Z_{in} and Z_{out} of an SRC with parameters listed in Table II. The simulation parameters have been taken from [16] and are simulated for two switching frequencies, one below resonance $f_s = 0.9f_o$ and one above resonance $f_s = 1.2f_o$. The simulated Bode plot is overlaid on top of the analytical models developed in this article, as shown in Figs. 4 and 5 .

As can be seen the model is able to accurately predict the small-signal behavior of SRC including the beat frequency dynamics, hence the model can be used even for high bandwidth controller design. Experimental verification of the model was also performed using an SRC with $L = 236\,\mu$H, $C = 0.475\,\mu$F, and $f_o = 15$ kHz.

The SRC was operated below resonance at $f_s = 14$ kHz resulting in a beat frequency of $f_o - f_s = 1$ kHz and above resonance at $f_s = 16.5$ kHz resulting in a beat frequency of $f_s - f_o = 1.5$ kHz. The SRC was driven with an FM gate driver signal, as shown in Fig. 6, wherein the quiescent frequency was set at the operating frequency, about which sinusoidal perturbations were provided with the frequency at which the control-to-output gain and phase needed to be observed. The sinusoidal

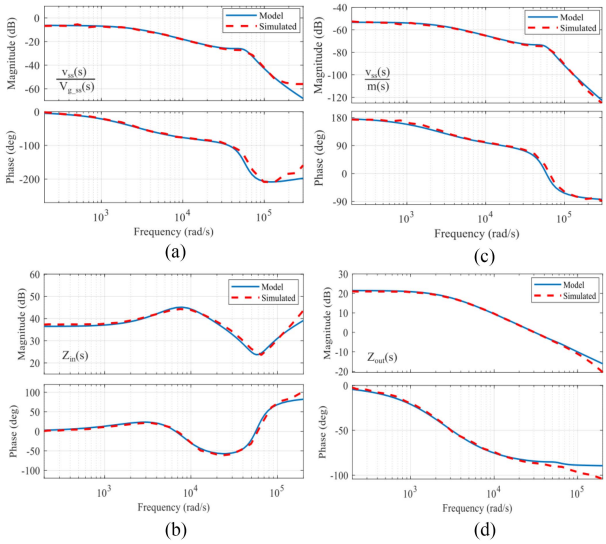

Fig. 5. Comparison of analytical model with simulated data for $f_s = 1.2f_o$. (a) Input to output tf. (b) Z_{in}. (c) Control to output transfer function. (d) Z_{out}.

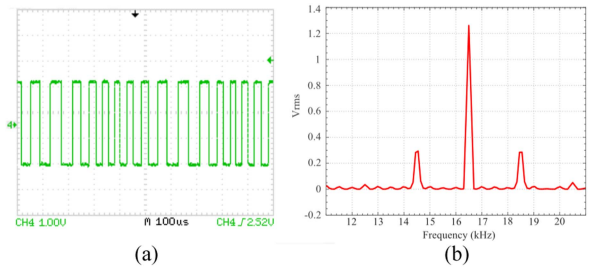

Fig. 6. (a) Exaggerated FM gate driver voltage. (b) FFT of gate driver voltage.

perturbations in frequency result in sinusoidal varying inductor current envelope and output voltage, as shown in Figs. 7 and 8, for different perturbation frequencies. As can be seen in Fig. 7(a), the perturbation in output voltage lags frequency perturbation by 30–40° when operated below resonance (14 kHz) and when the perturbation frequency (100 Hz) is small compared with beat frequency (1 kHz). The perturbation output voltage, however, lags frequency perturbation by 210–220° when operated above resonance (16.5 kHz) and when the perturbation frequency (200 Hz) is small compared with beat frequency (1.5 kHz), as shown in Fig. 8(a). This can also be seen from the steady-state gain curve of SRC [1], as presented in Fig. 9, where the slope below resonant frequency is positive (forward acting) while the slope above resonant frequency is negative (reverse acting). This corresponds exactly to the small-signal phase starting from 0° below resonance and 180° above resonance. The additional phase lag of 30–40° from 0° and 180°, as seen in the experimental plots, is introduced due to the pole formed by the filter capacitor C_f and the load resistor R at the output. It also reveals that if the SRC is designed to operate close to resonant frequency, care must be taken to stay entirely above or below the resonant frequency; otherwise, the abrupt change in phase can lead to closed-loop instability.

The output voltage perturbations were measured using a National Instruments data acquisition system to determine the magnitude gain and phase shift between the input frequency

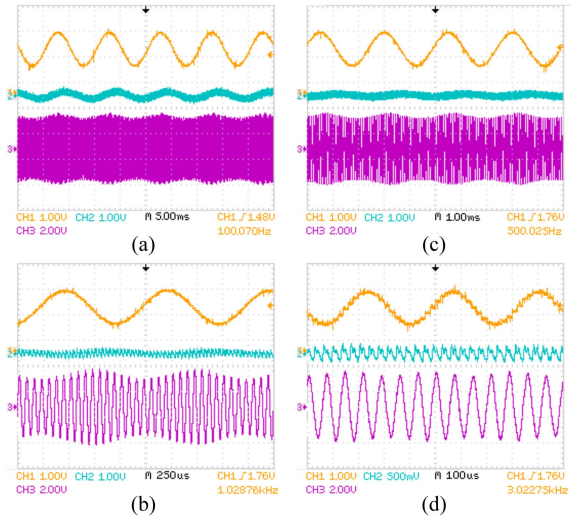

Fig. 7. Instantaneous frequency shown in orange (CH1), inductor current shown in purple (CH3), and output voltage perturbation shown in blue (CH2) for $f_s = 0.9333 f_o$. Perturbation frequency: (a) 100 Hz, (b) 1 kHz, (c) 500 Hz, and (d) 3 kHz.

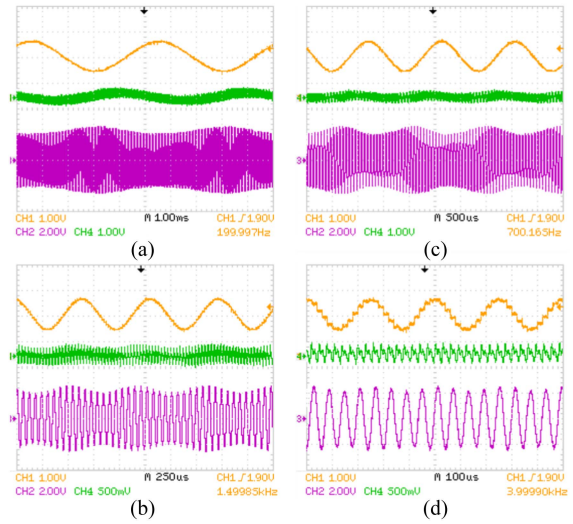

Fig. 8. Instantaneous frequency shown in orange (CH1), inductor current shown in purple (CH2), and output voltage perturbation shown in green (CH4) for $f_s = 1.1 f_o$. Perturbation frequency: (a) 200 Hz, (b) 700 Hz, (c) 1.5 kHz, and (d) 4 kHz.

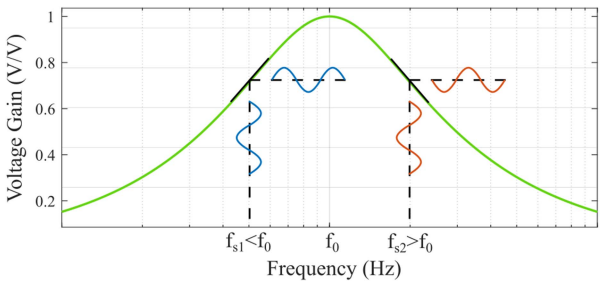

Fig. 9. Steady-state gain curve for the SRC.

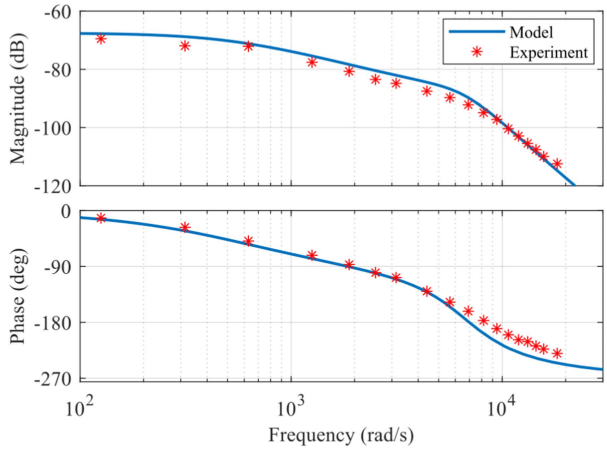

Fig. 10. Comparison of the analytical model with experimental data for $f_s = 0.9333 f_o$.

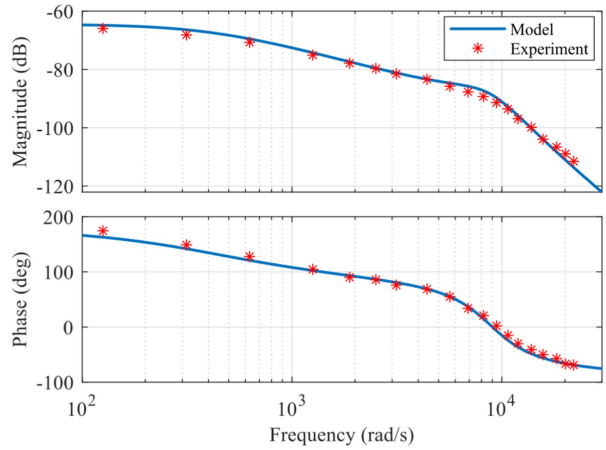

Fig. 11. Comparison of the analytical model with experimental data for $f_s = 1.1 f_o$.

TABLE III
PARAMETERS OF THE HARDWARE PROTOTYPE OF SRC

Parameter	Value
Input Nominal Voltage	80 V
Output maximum power	300 W
Resonant Frequency	16 kHz
Resonant Inductor (L)	197 μH
Resonant Capacitor (C)	0.5 μF
Filter Capacitor (C_f)	235 μF

perturbation and output voltage perturbation, hence providing a data point for the Bode plot. This experiment was performed at different perturbation frequencies to generate the experimental Bode plot. As can be seen from Figs. 10 and 11, the model matches the experimental results very well; the beat frequency dynamics are also captured as can be seen from the double pole present around the theoretical beat frequency.

A two-pole-one-zero controller [22] was designed for an SRC with specifications, as shown in Table III. The PI zero was placed at a frequency of 1300 rad/s, close to the RC_f pole of the system to ensure -20 dB/decade slope and close to -90° phase around gain crossover frequency of 3500 rad/s. To ensure that the resonant poles do not cause multiple gain crossovers and

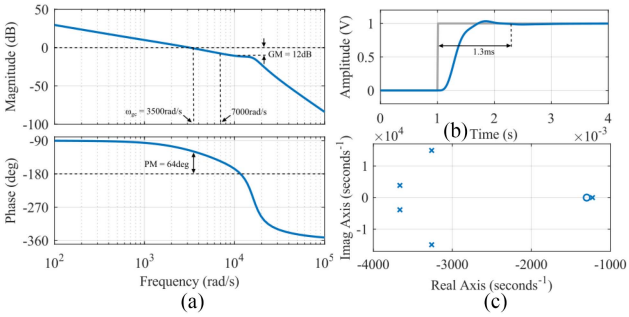

Fig. 12. (a) Loop gain of the compensated system. (b) Step response of the system. (c) Closed-loop pole-zero plot.

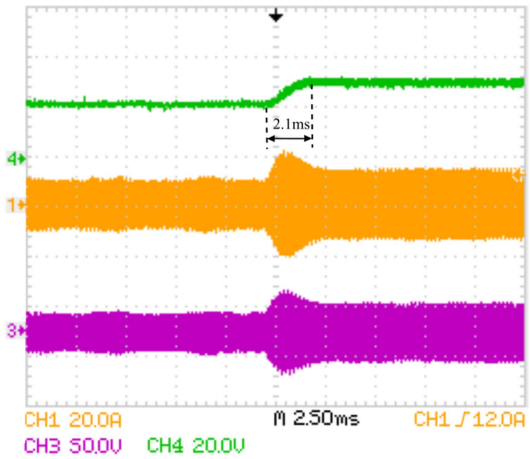

Fig. 13. Step response of SRC. Inductor current shown in orange (CH1), capacitor voltage (1:10) shown in purple (CH3), and output voltage shown in green (CH4).

high frequency ringing, another pole was added at 7000 rad/s. This reduced the phase margin to 64° but ensured a gain margin of 12 dB. The Bode plot of loop gain and transient response to step input are presented in Fig. 12. The experimental waveforms for the designed SRC are presented in Fig. 13. As can be seen, the output voltage accurately tracks the step change in reference, which closely matches with that predicted from the model. The slight increase in settling time is partly due to the reduced control-to-output gain of experimental setup compared with that predicted from the model, as seen in Figs. 10 and 11, and partly due to the inherent change in the small-signal model with change in operating frequency, as discussed in the next section.

V. Performance Analysis of SRC With the Derived Model

Resonant converters have been widely used in telecom industry that requires a fixed and regulated output voltage of 48 V [23]. Hence, a controller designed for a fixed output voltage is usually sufficient for operation. This controller, however, cannot be used for wide output voltage applications such as LED dimming, battery charging, and renewable energy systems. This is because the steady-state operating frequency has wide variation in such applications; hence, the small-signal model used to design the controller may not be valid over the entire range of operation and

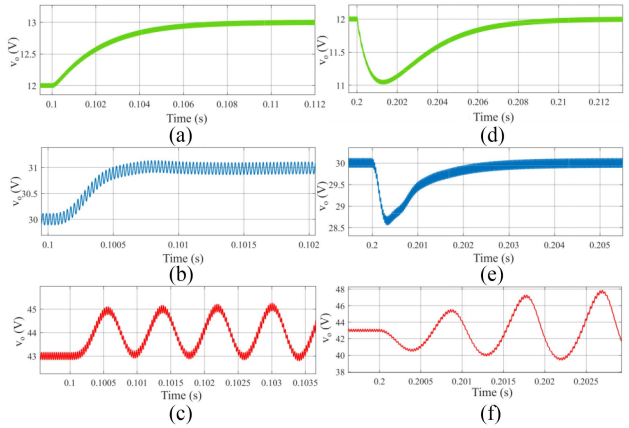

Fig. 14. System response analysis with change in operating point. Left: Output voltage response to unit step change in reference at 0.1 s. (a) 12 to 13 V (sluggish). (b) 30 to 31 V (expected/designed). (c) 43 to 44 V (unstable). Right: Output voltage response to input voltage step from 80 to 70 V at 0.2 s. (d) 12-V output (sluggish). (e) 30-V output (expected). (f) 43-V output (unstable).

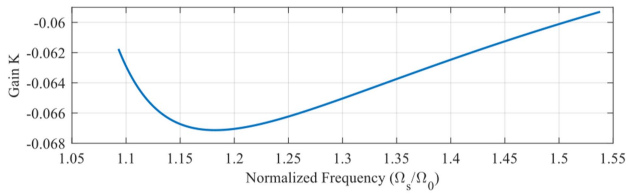

Fig. 15. Variation of gain K with operating frequency.

can cause stability or performance degradation. A performance analysis technique for such wide output voltage applications is presented below.

Considering the SRC with specifications presented in Table III, the output voltage is required to vary from 12 to 48 V with a nominal value of 30 V. The output voltage response of the system designed in Section IV to change in reference and input voltage is presented in Fig. 14. As can be seen, the output voltage is able to track step changes in reference at 30 V with desired bandwidth; however, the response at 12 V ($\Omega_s = 1.54\ \Omega_0$) is sluggish; also, the system becomes unstable at 44 V ($\Omega_s = 1.107\ \Omega_0$) and above. This happens because the small-signal model of SRC varies with change in operating frequency (indirectly change in reference voltage). The variation of closed-loop poles with varying operating frequency can be visualized with the help of root locus and small-signal transfer function developed in this article.

In (40), only the terms K and X_{eq} are dependent on operating frequency Ω_s, out of which the term K has a very weak dependence on Ω_s, as shown in Fig. 15, for the SRC parameters in Table III. Hence, the term K can be approximated to its average value of $K = -0.0635$ for the entire operating frequency range $\Omega_s = 1.094\Omega_0$ to $\Omega_s = 1.54\Omega_0$. The closed-loop transfer function for the SRC can be written as

$$G_{\text{cl}}(s) = \frac{G_c(s)G_p(s)}{1 + G_c(s)G_p(s)} \tag{43}$$

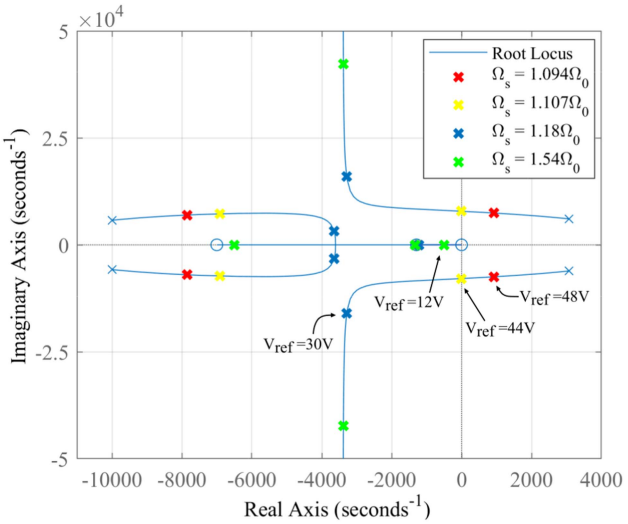

Fig. 16. Root locus of SRC with varying operating frequency and using a fixed controller.

where $G_c(s)$ is the controller transfer function, $G_p(s)$ is the plant transfer function, and G_{cl} is the closed-loop transfer function

$$G_{\text{cl}}(s) = \frac{G_c(s)K}{\text{den}_2(s) + G_c(s)K} \tag{44}$$

$$G_{cl}(s) = \frac{G_c(s)K/M(s)}{1 + X_{\text{eq}}^2(1 + RC_f s)/M(s)} \tag{45}$$

where $M(s) = (4L^2s^2 + 2R_{\text{eq}}Ls)(1 + RC_f s) + R_{\text{eq}}(2Ls + R_{\text{eq}}) + G_c(s)K$

Now, (45) is in the form used for root locus, where X_{eq}^2 is the variable gain dependent on the operating frequency, and the closed-loop poles of the system vary along the root locus of the term $\frac{(1+RC_f s)}{M(s)}$. X_{eq}^2 can be mapped back to Ω_s, which can then be mapped to a voltage reference V_{ref} to determine the limits of stable operation and performance. The root locus for the previously designed closed-loop system is shown in Fig. 16 with important locations marked. As can be seen, a pair of complementary poles are in the right half-plane for $V_{\text{ref}} = 48\,\text{V}$ resulting in an unstable system. The complementary pair of poles move toward higher frequency for $V_{\text{ref}} = 12\,\text{V}$; however, the single pole on the real axis moves closer to origin resulting in sluggish response at $V_{\text{ref}} = 12\,\text{V}$. The boundary between stable and unstable systems is given for $V_{\text{ref}} = 44\,\text{V}$ that is verified from the simulation as well. Hence, the simple and accurate model derived in this article can be readily used to predict the performance for wide output voltage application designs.

VI. Conclusion

This article presents the derivation of a third-order control-to-output transfer function of SRC. The derivation uses an intuitive approach of modeling the switching frequency variation as an FM voltage source and solving for the perturbations in inductor current envelope in the Laplace domain using the assumption that the perturbation frequency is much smaller than the switching frequency. Finally, the current envelope perturbations are related to output voltage perturbations to obtain the transfer function. Hence, the derivation does not involve complex mathematics or numerical solutions but simple algebraic manipulation that is extended to obtain the input-to-output transfer function, input impedance, and output impedance. The model is able to predict beat frequency dynamics as was validated with the help of simulated and experimental frequency response and, hence, can be used to design high-bandwidth controllers. The model can also be used for the analysis of wide output voltage application designs, as demonstrated in this article.

Appendix A
Derivation of Input-to-Output Transfer Function

The derivation of the input-to-output transfer function is similar to that of the control-to-output transfer function except the change in the model of switching network. Since the frequency is now fixed, it is no longer an FM voltage source; however, the dc voltage source is provided with a small-signal perturbation $V_g(t) = V_{g\_\text{dc}} + V_{g\_\text{ss}}(t)$ resulting in perturbation of square wave amplitude. Hence, the square wave can be represented using fundamental harmonic approximation as follows:

$$v_s(t) = \frac{4}{\pi}(V_{g\_\text{dc}} + V_{g\_\text{ss}})\cos(\Omega_s t). \tag{46}$$

Substituting $v_s(t)$ from (46), and $i_r(t) = (I_{c\_\text{dc}} + I_{c\_\text{ss}})\cos(\Omega_s t) + (I_{s\_\text{dc}} + I_{s\_\text{ss}})\sin(\Omega_s t)$ and $v_r(t)$ from (18) into (25), and performing harmonic balance result in two ODEs as before. The dc quantities are removed, both equations are converted to the Laplace domain, and I_{c_ss} and I_{s_ss} terms are grouped as follows:

$$\frac{4}{\pi}V_{g\_\text{ss}}(s)s = \Bigg(-L\Omega_s^2 + Ls^2 + \frac{1}{C} + R_{\text{eq}}\left(\beta^2 s - \alpha\beta\Omega_s\right) + \frac{R_{\text{eq}}}{RC_f s + 1}\left(\alpha^2 s + \alpha\beta\Omega_s\right)\Bigg) I_{c\_\text{ss}}(s) + \Bigg(2L\Omega_s s + R_{\text{eq}}\left(\alpha^2\Omega_s - \alpha\beta s\right) + \frac{R_{\text{eq}}}{RC_f s + 1}\left(\alpha\beta s + \beta^2\Omega_s\right)\Bigg) I_{s\_\text{ss}}(s) \tag{47}$$

$$-\frac{4}{\pi}V_{g\_\text{ss}}(s)\Omega_s = -\Bigg(2L\Omega_s s + \frac{R_{\text{eq}}}{RC_f s + 1}\left(\alpha^2\Omega_s - \alpha\beta s\right) + R_{\text{eq}}\left(\beta^2\Omega_s + \alpha\beta s\right)\Bigg) I_{c\_\text{ss}}(s) + \Bigg(-L\Omega_s^2 + Ls^2 + \frac{1}{C} + R_{\text{eq}}\left(\alpha^2 s + \alpha\beta\Omega_s\right) + \frac{R_{\text{eq}}}{RC_f s + 1}\left(\beta^2 s - \alpha\beta\Omega_s\right)\Bigg) I_{s\_\text{ss}}(s). \tag{48}$$

As before, v_{ss} has been substituted in terms of I_{c_ss} and I_{s_ss} using (23). Equations (47) and (48) can be divided by Ω_s, and the approximation $\frac{s}{\Omega_s} \approx 0$ can used to reduce the equations similar to (34) and (35). These two equations can then be solved to derive the perturbations in current envelopes I_{c_ss} and I_{s_ss} as

$$I_{c\_\text{ss}}(s) = \frac{4}{\pi}\frac{\left(2Ls + \alpha^2 R_{\text{eq}} + \beta^2\frac{R_{\text{eq}}}{RC_f s+1}\right)}{\text{den}_3}V_{g\_\text{ss}}(s) \tag{49}$$

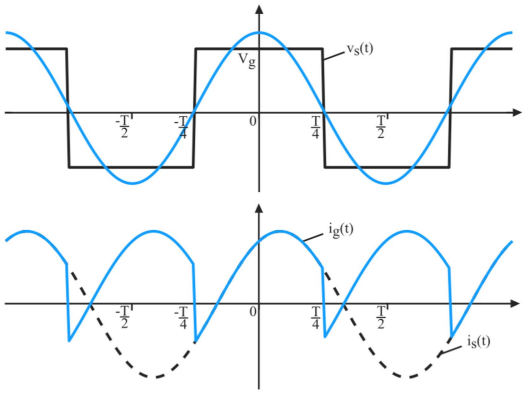

Fig. 17. Switching network voltage and current waveforms.

$$I_{s\_ss}(s) = \frac{4}{\pi}\frac{\left(X_{\text{eq}} + \alpha\beta R_{\text{eq}} - \alpha\beta\frac{R_{\text{eq}}}{RC_f s+1}\right)}{\text{den}_3} V_{g\_ss}(s) \quad (50)$$

where

$$\text{den}_3 = 4L^2s^2 + 2R_{\text{eq}}Ls + X_{\text{eq}}^2 + \frac{R_{\text{eq}}}{RC_f s+1}(2Ls + R_{\text{eq}}) \quad (51)$$

and X_{eq} is the same as before.

The small-signal variation in the inductor current envelope $I_{e\_ss}(s) = \alpha I_{c\_ss}(s) + \beta I_{s\_ss}(s)$ due to perturbation of input voltage source can be found as

$$I_{e\_ss}(s) = \frac{4}{\pi}\frac{1}{\sqrt{R_{\text{eq}}^2 + X_{\text{eq}}^2}}\frac{(X_{\text{eq}}^2 + R_{\text{eq}}^2 + 2LR_{\text{eq}}s)}{\text{den}_3} V_{g\_ss}(s). \quad (52)$$

The small-signal transfer function from $V_{g\_ss}(s)$ to $v(s)$ can be derived by substituting (52) into (23), as follows:

$$\frac{v_{\text{ss}}(s)}{V_{g\_ss}(s)} = \frac{K_1(X_{\text{eq}}^2 + R_{\text{eq}}^2 + 2LR_{\text{eq}}s)}{\text{den}_2} \quad (53)$$

where $K_1 = \frac{R_{\text{eq}}}{\sqrt{R_{\text{eq}}^2+X_{\text{eq}}^2}}$ and den_2, as given in (41).

Appendix B
Derivation of Converter Input Impedance

The input impedance of the converter can be easily derived using the results from the previous section. Given that the input voltage perturbations resulted in small-signal perturbations of output voltage and inductor current, the input small-signal current drawn by the converter $i_g(t)$ needs to be determined, and the ratio $\frac{V_{g\_ss}(s)}{i_{g\_ss}(s)}$ needs to be taken to derive the input impedance $Z_{\text{in}}(s)$. The input current $i_g(t)$ can be determined by averaging $i_s(t)$ in the time interval $[-\frac{T_s}{4}, \frac{T_s}{4}]$, as shown in Fig. 17. Given that $i_s(t) = i_r(t)$, we have

$$i_g(t) = \frac{2}{T_s}\int_{-\frac{T_s}{4}}^{\frac{T_s}{4}} i_r(\tau)\, d\tau \quad (54)$$

$$i_g(t) = \frac{2}{T_s}\int_{-\frac{T_s}{4}}^{\frac{T_s}{4}} I_c(t)\cos(\Omega_s\tau) + I_s(t)\sin(\Omega_s\tau)\, d\tau \quad (55)$$

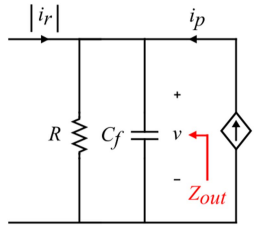

Fig. 18. Converter output impedance.

$$i_g(t) = \frac{2}{\pi}I_c(t) \quad (56)$$

where variation in $I_c(t)$ and $I_s(t)$ is assumed to be slow compared to averaging interval. This holds true if the perturbation frequency of $V_g(t)$ is small compared with the switching frequency. Hence, $i_{g\_ss}(s)$ can be determined by converting (56) to the Laplace domain and substituting I_{c_ss} from (49)

$$i_{g\_ss} = \frac{8}{\pi^2}\frac{\left(2Ls + \alpha^2 R_{\text{eq}} + \beta^2\frac{R_{\text{eq}}}{RC_f s+1}\right)}{\text{den}_3} V_{g\_ss}(s) \quad (57)$$

$$Z_{\text{in}}(s) = \frac{\pi^2}{8}\frac{\text{den}_2}{2Ls(RC_f s+1) + \alpha^2 R_{\text{eq}}RC_f s + R_{\text{eq}}^2}. \quad (58)$$

Appendix C
Derivation of Converter Output Impedance

The output impedance can be determined by attaching a small-signal current source to the output parallel load $R||C_f$. The current source produces terminal voltages such that it injects a small-signal current $i_p(t)$ into the converter. To determine the output impedance, first, the small-signal output voltage perturbations $v_{\text{ss}}(t)$ need to be determined and the ratio $\frac{v_{\text{ss}}(t)}{i_p(t)}$ needs to be taken in the Laplace domain. From Fig. 18, the output voltage equation can be written as

$$C_f\frac{dv(t)}{dt} + \frac{v(t)}{R} = i_p(t) + |i_r(t)| \quad (59)$$

$$v(s) = \frac{R}{(1+RC_f s)}\left(i_p(s) + \frac{2}{\pi}\left(\alpha I_{c\_ss}(s) + \beta I_{s\_ss}(s) + \frac{I_{e\_dc}}{s}\right)\right) \quad (60)$$

where $I_{e\_dc} = \sqrt{I_{c\_dc}^2 + I_{s\_dc}^2}$

Substituting $v_s(t) = \frac{4}{\pi}V_g\cos(\Omega_s t)$, $i_r(t) = (I_{c\_dc} + I_{c\_ss})\cos(\Omega_s t) + (I_{s\_dc} + I_{s\_ss})\sin(\Omega_s t)$, and $v_r(t)$ from (18) into (25) and performing harmonic balance result in two ODEs. The dc quantities are removed, both equations are converted to the Laplace domain, and I_{c_ss} and I_{s_ss} terms are grouped as follows:

$$-\frac{4R}{\pi(RC_f s+1)}(\alpha s + \beta\Omega_s)i_p(s) = (R_{\text{eq}}(\beta^2 s - \alpha\beta\Omega_s) + \frac{1}{C}$$
$$+L(s^2 - \Omega_s^2) + \frac{R_{\text{eq}}}{RC_f s+1}(\alpha^2 s + \alpha\beta\Omega_s))I_{c\_ss}(s) + (2L\Omega_s s$$
$$+ R_{\text{eq}}(\alpha^2\Omega_s - \alpha\beta s) + \frac{R_{\text{eq}}}{RC_f s+1}(\alpha\beta s + \beta^2\Omega_s))I_{s\_ss}(s) \quad (61)$$

$$-\frac{4R}{\pi(RC_f s+1)}(\beta s-\alpha\Omega_s)i_p(s)=-(2L\Omega_s s+R_{\text{eq}}(\beta^2\Omega_s+\alpha\beta s)+\frac{R_{\text{eq}}}{RC_f s+1}(\alpha^2\Omega_s-\alpha\beta s))I_{c\_ss}(s)+(L(s^2-\Omega_s^2)+\frac{1}{C}+R_{\text{eq}}(\alpha^2 s+\alpha\beta\Omega_s)+\frac{R_{\text{eq}}}{RC_f s+1}(\beta^2 s-\alpha\beta\Omega_s))I_{s\_ss}(s). \tag{62}$$

As before, v_{ss} has been substituted in terms of I_{c_ss} and I_{s_ss} using (23). Equations (61) and (62) are similar to (47) and (48) except for the change in perturbation source. These two equations can then be solved to derive the perturbations in current envelopes I_{c_ss} and I_{s_ss} as

$$I_{c\_ss}(s)=-\frac{4}{\pi}\frac{R(2\alpha Ls+\alpha R_{\text{eq}}-\beta X_{\text{eq}})}{\text{den}_2}i_p(s) \tag{63}$$

$$I_{s\_ss}(s)=-\frac{4}{\pi}\frac{R(2\beta Ls+\beta R_{\text{eq}}+\alpha X_{\text{eq}})}{\text{den}_2}i_p(s) \tag{64}$$

$$I_{e\_ss}=\alpha I_{c\_ss}(s)+\beta I_{s\_ss}(s)=-\frac{4}{\pi}\frac{R(2Ls+R_{\text{eq}})}{\text{den}_2}i_p(s). \tag{65}$$

Now, $v_{\text{ss}}(s)$ can be determined easily as

$$v_{\text{ss}}(s)=\frac{R}{RC_f s+1}(i_p(s)+\frac{2}{\pi}(\alpha I_{c\_ss}(s)+\beta I_{s\_ss}(s))) \tag{66}$$

$$v_{\text{ss}}(s)=\frac{R(4L^2s^2+2R_{\text{eq}}Ls+X_{\text{eq}}^2)}{\text{den}_2}i_p(s) \tag{67}$$

$$Z_{\text{out}}(s)=\frac{R(4L^2s^2+2R_{\text{eq}}Ls+X_{\text{eq}}^2)}{\text{den}_2}. \tag{68}$$

REFERENCES

[1] W. R. Erickson and D. Maksimovic, *Fundamentals of Power Electronics*. New York, NY, USA: Springer, 2007.

[2] J. E. Huber, D. Rothmund, and J. W. Kolar, "Comparative evaluation of isolated front end and isolated back end multi-cell SSTs," in *Proc. IEEE 8th Int. Power Electron. Motion Control Conf.*, 2016, pp. 3536–3545.

[3] S. Inoue and H. Akagi, "Voltage control of a bi-directional isolated dc/dc converter for medium-voltage motor drives," in *Proc. Power Convers. Conf.*, 2007, pp. 1244–1250.

[4] D. M. Bellur and M. K. Kazimierczuk, "DC-DC converters for electric vehicle applications," in *Proc. Elect. Insul. Conf. Elect. Manuf. Expo*, 2007, pp. 286–293.

[5] L. Huber and M. M. Jovanovic, "A design approach for server power supplies for networking applications," in *Proc. 15th Annu. IEEE Appl. Power Electron. Conf. Expo.*, 2000, pp. 1163–1169.

[6] B. S. Nathan and V. Ramanarayanan, "Analysis, simulation and design of series resonant converter for high voltage applications," in *Proc. IEEE Int. Conf. Ind. Technol.*, 2000, pp. 688–693.

[7] Z. U. Zahid, Z. M. Dalala, R. Chen, B. Chen, and J.-S. Lai, "Design of bidirectional dc–dc resonant converter for vehicle-to-grid (V2G) applications," *IEEE Trans. Transp. Electrific.*, vol. 1, no. 3, pp. 232–244, Oct. 2015.

[8] R. D. Middlebrook and S. Cuk, "A general unified approach to modelling switching-converter power stages," in *Proc. IEEE Power Electron. Spec. Conf.*, 1976, pp. 18–34.

[9] V. Vorpérian, "Simplified analysis of PWM converters using model of PWM switch. II. Discontinuous conduction mode," *IEEE Trans. Aerosp. Electron. Syst.*, vol. 26, no. 3, pp. 497–505, May 1990.

[10] F. D. Tan and R. D. Middlebrook, "A unified model for current-programmed converters," *IEEE Trans. Power Electron.*, vol. 10, no. 4, pp. 397–408, Jul. 1995.

[11] J. Li and F. C. Y. Lee, "Modeling of V^2 current-mode control," in *Proc. 24th Annu. IEEE Appl. Power Electron. Conf. Expo.*, 2009, pp. 298–304.

[12] V. Vorperian and S. Cuk, "Small signal analysis of resonant converters," in *Proc. IEEE Power Electron. Spec. Conf.*, 1983, pp. 269–282.

[13] M. E. Elbuluk, G. C. Verghese, and J. G. Kassakian, "Sampled-data modeling and digital control of resonant converters," *IEEE Trans. Power Electron.*, vol. 3, no. 3, pp. 344–354, Jul. 1988.

[14] R. J. King and T. A. Stuart, "Small-signal model for the series resonant converter," *IEEE Trans. Aerosp. Electron. Syst.*, vol. AES-21, no. 3, pp. 301–319, May 1985.

[15] E. X. Yang, F. C. Lee, and M. M. Jovanovic, "Small-signal modeling of series and parallel resonant converters," in *Proc. 7th Annu. Appl. Power Electron. Conf. Expo.*, 1992, pp. 785–792.

[16] S. Tian, F. C. Lee, and Q. Li, "A simplified equivalent circuit model of series resonant converter," *IEEE Trans. Power Electron.*, vol. 31, no. 5, pp. 3922–3931, May 2016.

[17] S. J. T. G. and V. John, "Circuit-parameter-based audiosusceptibility model for series resonant converter," *IEEE Trans. Power Electron.*, vol. 34, no. 6, pp. 5927–5939, Jun. 2019.

[18] X. Li, Y. Zhang, S. Chen, X. Zhang, and Y. Tang, "General multi-frequency small-signal model for resonant converters," *IEEE Trans. Power Electron.*, vol. 37, no. 4, pp. 3892–3912, Apr. 2022.

[19] *Survey of Resonant Converter Topologies*, Power Supply Design Seminar, 2018.

[20] U. Madhow, *Introduction to Communication Systems*. Cambridge, U.K.: Cambridge Univ. Press, 2014.

[21] V. Vorperian, "Approximate small-signal analysis of the series and the parallel resonant converters," *IEEE Trans. Power Electron.*, vol. 4, no. 1, pp. 15–24, Jan. 1989.

[22] S. S. Chakraborty and K. Hatua, "Modeling with beat frequency dynamics and phase-frequency control design for a dual-bridge series resonant converter," *IEEE Trans. Ind. Electron.*, vol. 69, no. 8, pp. 7952–7962, Aug. 2022.

[23] J. Biela, U. Badstuebner, and J. W. Kolar, "Design of a 5-kW, 1-U, 10-kW/dm^3 resonant dc–dc converter for telecom applications," *IEEE Trans. Power Electron.*, vol. 24, no. 7, pp. 1701–1710, Jul. 2009.

Soumitro Vyapari received the B.Tech. degree in electrical engineering from the Indian Institute of Technology Tirupati, Tirupati, India, in 2022.

He is currently an Analog Engineer with Texas Instruments, Bengaluru, India. His current research interests include modeling and control of resonant converters.

Viju Nair R (Member, IEEE) received the B.Tech. degree in electrical and electronics engineering from Mar Athanasius College of Engineering, Kothamangalam, India, in 2009, the M.Tech. degree in electrical engineering with specialization in power electronics and power systems from the Indian Institute of Technology Bombay, Mumbai, India, in 2013, and the Ph.D. degree in power electronics from the Indian Institute of Science, Bengaluru, India, in 2018.

He received the postdoctoral fellowship from the FREEDM Systems Center, Raleigh, NC, USA. His current research interests include high-power converters for motor drives, grid integration of renewable energy sources, soft switching, resonant conversion, and high-frequency magnetics.

Goutam Ghosh received the B.Tech. degree in electrical engineering from the Calcutta Institute of Engineering and Management, Kolkata, India, in 2019. He is currently working toward the Master of Science Research (M.S.) degree in power electronics with the Department of Electrical Engineering, Indian Institute of Technology Tirupati, Tirupati, India.

His current research interests include modeling and control of power converters, resonant converters, stability of power electronic converters, and dc fast chargers for electric vehicles.